2020-7

Rotor-on-Rotor Aeroacoustic Interactions of Multirotor in Hover

Eduardo Alvarez
Brigham Young University, ealvarez@byu.edu

Austin Schenk
Brigham Young University, austinschenkbyu@gmail.com

Tyler Critchfield
Brigham Young University, trcritchfield@gmail.com

Andrew Ning
Brigham Young University, aning@byu.edu

Rotor-on-Rotor Aeroacoustic Interactions of Multirotor in Hover

Eduardo J. Alvarez Doctoral Candidate
Austin Schenk Graduate Student
Tyler Critchfield Doctoral Candidate
Andrew Ning Associate Professor
Brigham Young University
Provo, UT, USA

ABSTRACT

Multirotor configurations introduce complicated aerodynamic and aeroacoustic interactions that must be considered during aircraft design. In this paper we explore two numerical methods to model the acoustic noise caused by aerodynamic rotor-on-rotor interactions of rotors in hover. The first method uses a conventional mesh-based unsteady Reynolds-average Navier-Stokes (URANS) solver, while the second consists of a meshless Lagrangian solver based on the viscous vortex particle method (VPM). Both methods are coupled with an aeroacoustics solver for tonal and broadband noise predictions. Noise predictions are validated for single and multi-rotor configurations, obtaining with the VPM a similar accuracy than URANS while being two orders of magnitude faster. We characterize the interactions of two side-by-side rotors in hover as the tip-to-tip distance and downstream spacing are varied. At an observer located six diameters away, multirotor noise is the strongest above and below the rotors, increasing by about 10 dBA directly underneath as the rotors are brought closer together. The interactions show no sensitivity to blade loading distribution, indicating that multirotor interactions are not alleviated with a lighter tip loading. We found that noise can be mitigated by spacing the rotors in the downstream direction—with the optimal spacing being about half a diameter—achieving a noise decrease of about 4 dBA without any aerodynamic penalties.

NOTATION

c	chord length, m
C_T	thrust coefficient, $C_T = \frac{T}{\rho n^2 D^4}$
d	tip-to-tip distance between rotors, m
D	rotor diameter, m
p'	acoustic pressure, Pa
r	radial position, m
R	rotor radius, m
Re_c	chord-based Reynolds number, $\mathrm{Re}_c = \frac{V_{70\%}\bar{c}}{\nu}$
Re_D	diameter-based Reynolds number, $\mathrm{Re}_D = \frac{V_{70\%}D}{\nu}$
s	downstream spacing between rotors, m
t	time, s
T	thrust, N
$\mathbf{u}$	velocity, m/s
U_z/U_{tip}	Axial velocity normalized by tip velocity
$V_{70\%}$	effective velocity at 70% blade span, m/s
$\mathbf{x}$	position, m
x	Leading edge position from blade centerline, m
y^+	Non-dimensional wall distance
z	Leading edge position from plane of rotation, m
Γ	vortex strength, m^3/s
ν	kinematic viscosity, m^2/s
ω	vorticity, $1/\mathrm{s}$
ρ	density, kg/m^3
ζ_σ	radial basis function, $1/\mathrm{m}^3$
$\bar{\square}^2$	wave-equation operator

INTRODUCTION

Electric propulsion has made possible the use of multiple rotors for electric vertical takeoff and landing (eVTOL). Many next-generation aircraft concepts include eVTOL capabilities, ranging from heavy lift quadcopters for payload delivery to passenger vehicles for urban air mobility, exemplified in Fig. 1. However, multirotors introduce complicated aerodynamic and aeroacoustic interactions that must be considered during design. For instance, recent research indicates

Figure 1: Novel eVTOL aircraft using multirotor configurations: (top) NASA GL-10 tilt-wing and (bottom) Army CRC-20 biplane tailsitter. Credits: NASA Langley/David C. Bowman and Ref. 1.

that aerodynamic rotor-on-rotor interactions in hover lead to a penalty in thrust as large as 4% (Refs. 2–4). This is also accompanied by a drastic increase in thrust fluctuations (about 250% higher than an isolated rotor) and a significant noise increase as the distance between rotors is decreased (Ref. 5).

Much research has been done in understanding and mitigating the acoustic noise of helicopter rotors; however, the smaller rotors used in eVTOL operate at a much lower Reynolds number and higher blade-passing frequency. This adds a strong broadband component to the tonal noise encountered in conventional rotorcraft (Ref. 6). Furthermore, aerodynamic rotor-on-rotor interactions in hover add a noise source in the form of unsteady loading that is unique to multirotor operation (Ref. 5).

In this paper we explore two numerical methods to model the noise caused by the aerodynamic rotor-on-rotor interactions of two side-by-side rotors in hover. The first method uses a conventional mesh-based unsteady Reynolds-average Navier-Stokes (URANS) solver, while the second consists of a meshless Lagrangian solver based on the viscous vortex particle method (VPM). The URANS approach aims to use moderate computing resources as would be available at a large company, while the VPM approach aims to use low computing resources available in everyday-use computers. The time-resolved aerodynamic solution obtained from either URANS or VPM is then used to calculate aeroacoustic tonal noise through the Ffowcs Williams-Hawkings (FW-H) acoustic analogy, and the broadband noise component is calculated through the Brooks, Pope, and Marcolini (BPM) equations. In this study, we present validation of both methods and identify their strengths. We characterize the relation between thrust fluctuations and noise caused by rotor-on-rotor interactions through a sweep of tip-to-tip distance and downstream spacing between rotors. In order to explore the effects of blade loading distribution, we perform these sweeps with two sets of rotors: one set that is heavily loaded towards the blade tip, while the other set distributes the load inboard on the blade. The end result is a detailed study of rotor-on-rotor interactions (comprised of more than 25 URANS simulations) identifying best practices for modeling and mitigating multirotor aeroacoustic noise during aircraft design.

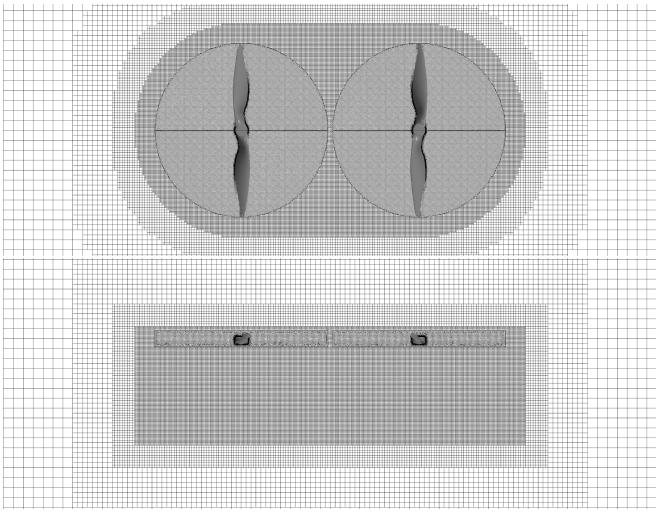

Figure 2: Front and top view of mesh around rotors.

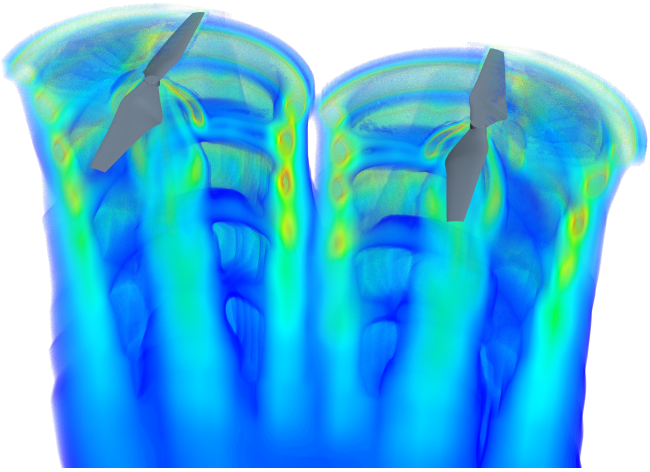

Figure 3: URANS simulation of rotors in hover depicting vorticity isovolumes.

MODELING METHODOLOGY

URANS Simulation

The URANS simulation approach uses an unsteady compressible solver with the SST k–ω turbulence model and all-y^+ wall treatment through the commercial code STAR-CCM+. The mesh uses both cuboid and polyhedral cells in a bullet-shape domain $40D$ in diameter that extends $40D$ and $80D$ in front and downstream of the rotors, respectively. The cells are refined down to a y^+ of 30 at each blade surface, the rotation is captured through a rotating mesh surrounding each rotor, and an exterior box of refinement is defined extending half a diameter downstream of the backmost rotor to resolve the wake, as shown in Fig. 2. This results in a mesh of 14 million cells. Temporal integration is done in a first-order scheme with time steps equivalent to 3° of rotor rotation, resolving 50 revolutions by the end of the simulation. Notice that this spatial and temporal discretization is in the lower-fidelity end relative to similar studies in the literature (Refs. 2, 7–11). We have chosen this discretization in order to explore whether rotor-on-rotor interactions can be accurately predicted with the limited computing resources that are typically available to the industry. The computation is performed using 192 CPU cores at BYU's Fulton supercomputer, requiring a wall-clock time of about 48 hours, equivalent to about 9200 processor hours. For more details about the solver and a convergence study, the reader is referred to parts of the Masters Thesis associated with this study (Ref. 12). Fig. 3 shows a slice of the vorticity isovolumes resulting from the simulation.

VPM Simulation

The viscous vortex particle method is a meshfree approach for solving the Navier-Stokes equations in their vorticity form,

$$\frac{D\omega}{Dt} = (\omega \cdot \nabla)\mathbf{u} + \nu\nabla^2\omega.$$

This form is especially well fitted for resolving wake dynamics since this type of flow is dominated by vorticity. The method consists in discretizing the vorticity field into Lagrangian elements (called vortex particles) using a radial basis function approximation of basis ζ_σ and coefficients Γ_p:

$$\omega(\mathbf{x},t) \approx \sum_p \Gamma_p(t)\zeta_\sigma(\mathbf{x}-\mathbf{x}_p(t)).$$

Each particle then represents a volume of fluid transporting vorticity as it travels with the local velocity. For a more detailed description of the method, the reader is referred to Refs. 13, 14. In summary, the VPM is a numerical method that efficiently preserves vortical structures in a Lagrangian scheme, eliminates the complexities of mesh generation, is absent of the numerical dissipation associated with mesh-based methods, and is one to three orders of magnitude faster than URANS.

This study will use the solver FLOWVPM developed by the authors in previous work (Refs. 4, 15, 16). This code has been integrated into FLOWUnsteady,[1] an open-source suite of mixed-fidelity unsteady aerodynamics and aeroacoustics simulations (Ref. 17). Evolution, mixing, and viscous diffusion of the wake is solved through the VPM, while aerodynamic and viscous forces on the blade are computed through blade elements, as explained in Ref. 16. Temporal integration is performed in a third-order scheme with time steps equivalent to 5° of rotor rotation, shedding particles every 2.5°, and resolving 50 revolutions by the end of the simulation. The computation is performed using 32 CPU cores in a desktop computer Intel® Xeon® CPU E5-2699 v3 @ 2.30 GHz, requiring a wall-clock time of about two hours, equivalent to about 64 processor hours. This results in a VPM simulation that is 140 times (or two orders of magnitude) faster than the URANS simulation, making it feasible to run this analysis in an every-day use desktop/laptop computer. As an example, Fig. 4 shows a VPM simulation of two side-by-side rotors in hover.

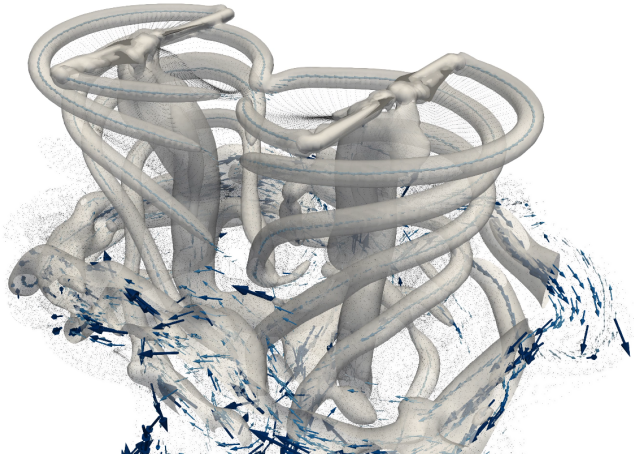

Figure 4: VPM simulation of rotors in hover depicting vorticity isosurfaces. Dots show the position of the particles, and arrows show the vortex strength Γ_p of every particle.

[1] https://github.com/byuflowlab/FLOWUnsteady

Aeroacoustics Solver

High-fidelity approaches for the prediction of aeroacoustic noise can be derived from the application of an acoustic analogy to the Navier-Stokes equations. One popular analogy for the calculation of rotor noise is known as the Ffowcs Williams-Hawkings (FW-H) analogy, that reduces the Navier-Stokes equations to

$$\bar{\Box}^2 p'(\mathbf{x},t) = \frac{\partial}{\partial t}\left(\rho_0 \mathbf{u}_n \delta(f)\right) - \frac{\partial}{\partial x_i}\left(\Delta P_{ij}\hat{\mathbf{n}}_j \delta(f)\right),$$

where $\bar{\Box}^2$ is the wave-equation operator, p' is the acoustic pressure, $\hat{\mathbf{n}}_j$ is the unit normal vector away from the blade surface, and $\Delta P_{ij} = (p - p_0)\delta_{ij}$. The first term in the right-hand side is a monopole source representing the volume displaced by the thickness of a solid body, the second term is a dipole source representing the force applied on the fluid by that body, and higher-order terms (quadrupole sources) have been neglected. This analogy has been shown to accurately predict helicopter noise radiated from complicated aerodynamic phenomena like blade-vortex interaction and high-speed impulsive effects (Ref. 18); however, it has not been extensively applied to the prediction of rotor-on-rotor aeroacoustic interactions. In a recent study, Zolbayar (Ref. 19) coupled FW-H with blade-element momentum theory to investigate the noise of a light airplane with distributed propulsion. He was able to draw conclusions about the accumulation of noise directivity, but he recognized the need of a higher-fidelity aerodynamic solver in order to capture important sources of noise associated with rotor-on-rotor and wing-on-rotor interactions. Thus, in this study we explore whether the increased noise due to rotor-on-rotor interactions can be predicted by coupling URANS or VPM with the FW-H equation.

Tonal noise is calculated in this study through the FW-H code PSU-WOPWOP, using the aerodynamic solution from either URANS or VPM. Ten rotor revolutions with time steps equivalent to 3° of rotation are used from the URANS solution, while the noise with VPM uses five rotor revolutions with time steps of 5°. The thickness noise component is calculated over the lofted blade geometry, while the loading noise component is calculated over compact patches. Analyses using mesh-based methods like URANS more frequently employ surface pressures rather than compact patches, but we have chosen to employ the latter since it makes the comparison of load distribution and load fluctuations more natural.

Broadband noise is calculated in this study through the Brooks, Pope, and Marcolini (BPM) method (Ref. 20), capturing noise from turbulent boundary layer edge, separation stall,

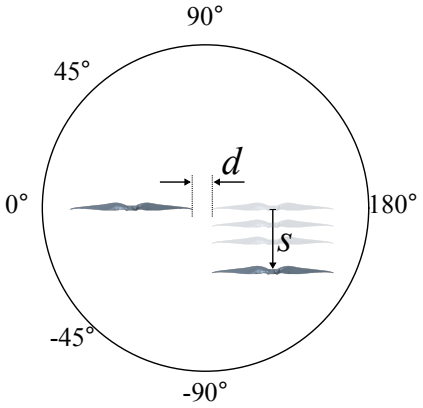

Figure 5: Tip-to-tip distance d, downstream spacing s, and microphone positions (not shown to scale).

tip vortex formation, laminar boundary layer vortex shedding, and trailing edge bluntness vortex shedding. The study uses an in-house developed BPM code.[2]

Test Cases

This study aims to characterize the rotor-on-rotor interactions of two counter-rotating, side-by-side rotors in hover as the tip-to-tip distance d and downstream spacing s are varied, as shown in Fig. 5. Three different two-bladed rotor geometries are used: the DJI 9443 used in Ref. 6 (9.4 inches diameter and 0.11), the DJI-like rotor used in Refs. 5,21 (9.4 inches diameter and 0.12 solidity), and the thin-electric APC 10x7 used in Ref. 22 (10 inches diameter and 0.10 solidity). The DJI-like rotor is hereon referred as Ning DJI. The Ning DJI rotor uses a uniform E63 airfoil shape transitioning to an E856 airfoil towards the hub, the APC 10x7 uses a NACA 4412 transitioning to a Clark Y towards the hub, while the airfoil sections of the DJI 9443 were obtained by digitizing slices of the actual rotor.Twist and chord distributions, along with leading edge curves are shown in Fig. 6. All rotors operate at a tip Mach close to 0.2 and chord-based and diameter-based Reynolds number (Re_c and Re_D) of approximately 6×10^4 and 7×10^5, respectively. Acoustics are calculted with a reference pressure of 2×10^{-5} Pa. Unless otherwise indicated, all observers are placed over a circular array of microphones located at a distance of $6D$ from the plane of symmetry as shown in Fig. 5.

SINGLE-ROTOR VALIDATION

Prior to testing the ability to capture rotor-on-rotor interactions, both simulation approaches are first validated for a single rotor. This is done by comparing to the experimental measurements of the DJI 9443 rotor in hover reported by Zawodny et al. (Ref. 6). The rotor is operated at 5400 RPM, resulting in a blade-passing frequency (BPF) of 180 Hz. The measurements are taken over a circular array of microphones located a distance of $7.9D$ from the rotor hub. Fig. 7 shows the convergence of the simulations along the experimental mean C_T—

[2] https://github.com/byuflowlab/BPM.jl

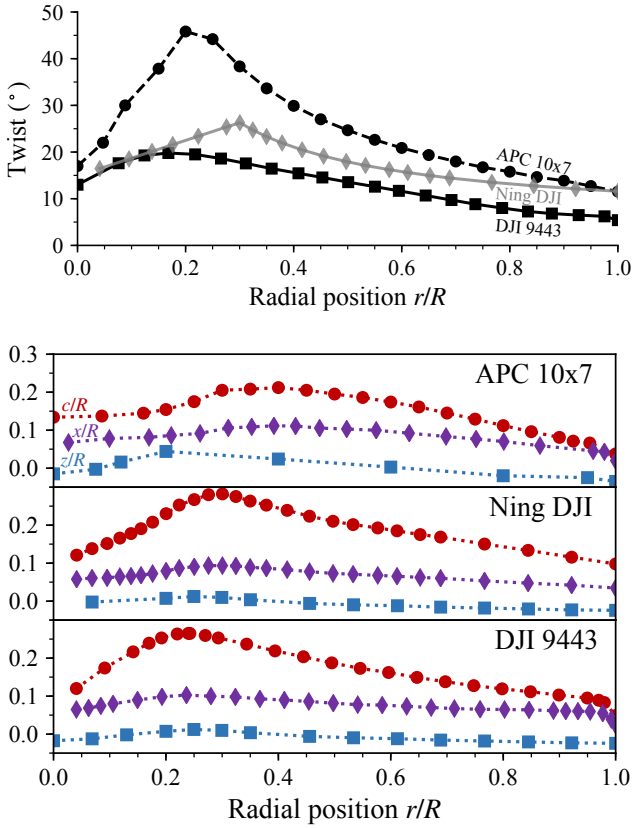

Figure 6: Twist distribution (top) and chord distribution along with leading edge curve (bottom) of each rotor.

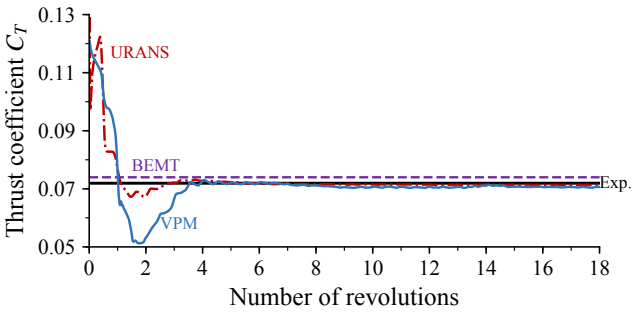

Figure 7: Convergence of single-rotor DJI 9443 simulations compared to experimental C_T.

which is 0.072—, resulting in discrepancies less than 2% relative to the experimental value.

Results in this section also include predictions using blade-element momentum theory (Refs. 23, 24)—or BEMT—implemented in the opensource code CCBlade.[3] This low-fidelity approach is as accurate as the high-fidelity VPM and URANS approaches when analyzing an isolated rotor, but it is not so in multirotor configurations where rotor-on-rotor interactions are predominant.

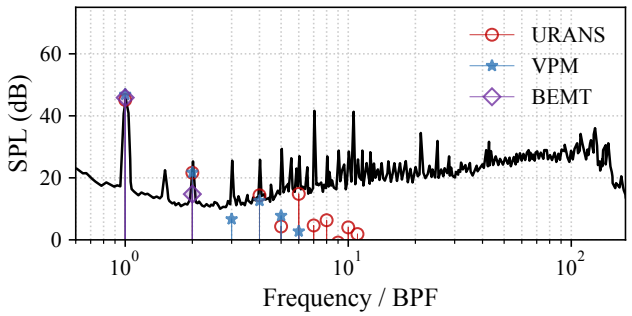

Figure 8: Experimental acoustic spectrum of the DJI 9443 single-rotor (measured at −45° microphone) compared to tonal predictions.

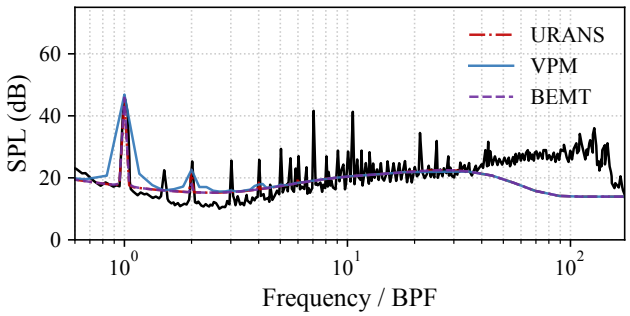

Figure 10: Predicted spectra of the DJI 9443 single-rotor (at −45° microphone) compared to experimental acoustic spectrum (black line).

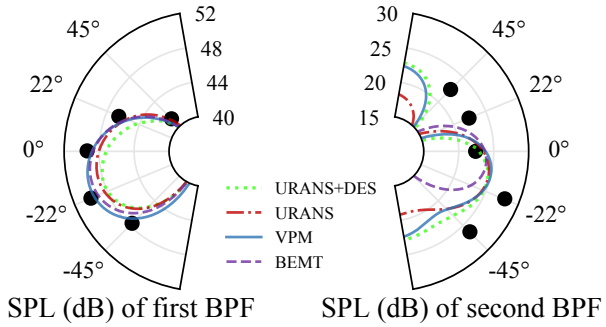

Figure 9: Tonal directivity predictions of DJI 9443 single-rotor compared to experimental measurements (black markers).

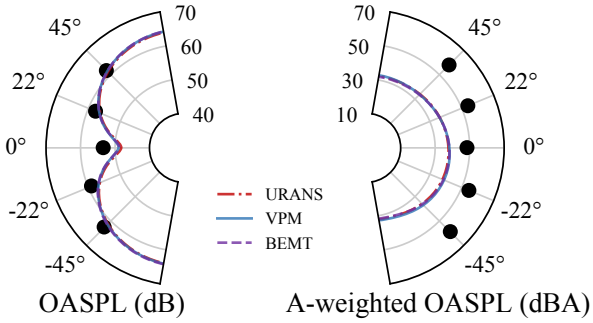

Figure 11: Unweighted and A-weighted OASPL directivity predictions of DJI 9443 single-rotor compared to experimental measurements (black markers).

Tonal Noise

The experimental spectrum (Ref. 6) recorded by the microphone at −45° below the plane of rotation is shown in Fig. 8 and is compared to the tonal noise calculated through the FW-H solver. Though the simulations miss the high-frequency content, they all successfully predict the sound pressure level (SPL) of the first BPF. Also, both VPM and URANS predict the SPL of the second BPF with reasonable accuracy (within 5 dB), while BEMT is about 10 dB off. The tonal directivity of both the first and second BPF is shown in Fig. 9, which also includes predictions obtained through the URANS detached-eddy simulation (DES) code OVERFLOW2 reported by Zawodny et al. (Ref. 6). OVERFLOW2 uses a high-order numerical scheme that is significantly more accurate than our URANS simulation, requiring 1008 CPU cores and more than six days of computation to resolve five rotor revolutions.[4] In the left figure it is observed that, in all directions, both URANS and URANS+DES are at most in between 2 dB from the experimental SPL of the first BPF, while the VPM is between 1 dB. In the right is observed that all simulations—including the high-fidelity URANS+DES—have discrepancies in the directivity pattern of the second BPF compared to the experimental. Though, the VPM shows good agreement with the URANS+DES simulation, making it a promising method for obtaining high-fidelity predictions at a significantly low computational cost.

Broadband Noise

Broadband noise calculated through BPM is then added to the tonal noise, as shown in shown in Fig. 10, matching the floor SPL of the high-frequency content with reasonable accuracy. Here it is seen that only the first and second BPF of the tonal component play a significant contribution to the total noise after adding the broadband component. Recent work has shown that some of the large SPL peaks observed experimentally in the higher BPFs are caused by motor noise[5] (Ref. 6) and small fluctuations of RPM (Ref. 25) that are not modeled in our simulations. The overall SPL (OASPL) directivity is shown in Fig. 11. In the left figure it is observed that the unweighted OASPL is accurately predicted by all methods, with the error being the largest (∼4 dB) at the plane of rotation. In the right figure there is a large discrepancy between the experimental and predicted A-weighted OASPL due to the high-frequency SPL peaks associated with motor noise and RPM fluctuations introduced in the experiment.

[3] https://github.com/byuflowlab/CCBlade.jl

[4] This is equivalent to about 150000 processor hours. In contrast, the VPM takes about two hours (equivalent to 64 processor hours) to resolve 50 revolution, making the VPM three orders of magnitude faster than URANS+DES.

[5] For instance, the SPL peak at the seventh BPF is associated to the number of magnetic poles, which is fourteen.

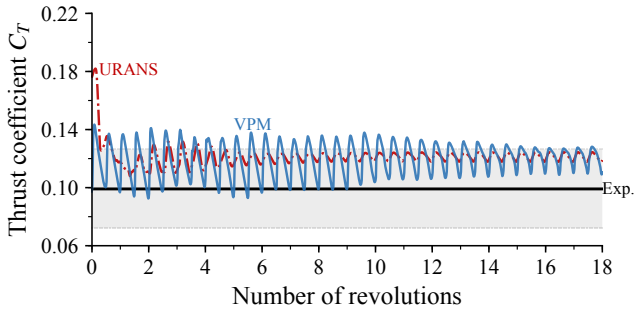

Figure 12: Instantaneous C_T of multirotor Ning DJI simulations at $d = 0.05D$ compared to experimental mean C_T. Shaded region encloses the experimental standard deviation.

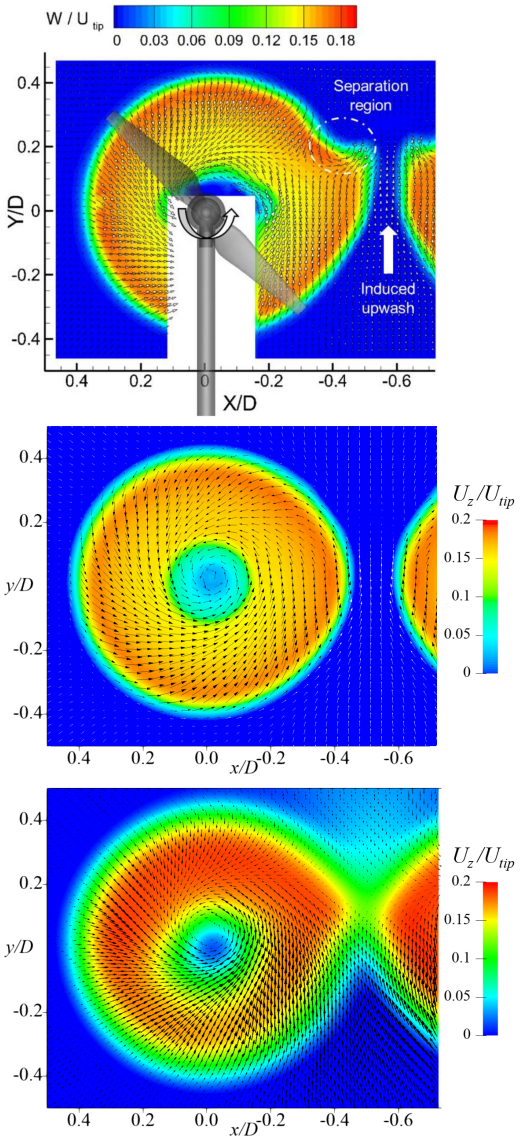

Figure 13: Velocity field of Ning DJI multirotor at a tip-to-tip distance $d = 0.05D$ as measured experimentally (top, retrieved from Ref. 5) and predicted by URANS (middle) and VPM (bottom).

MULTIROTOR RESULTS

Aerodynamic Interactions

Rotor-on-rotor interactions captured in our simulations are validated by comparing to the experimental measurements reported by Zhou et al. (Ref. 5) They measured the performance of two counter-rotating Ning DJI rotors when they are at a tip-to-tip distance d of $1D$ and when this distance is reduced to only $0.05D$. In all cases, the Ning DJI rotor is operated at 4860 RPM, resulting in a blade-passing frequency of 162 Hz. First, we must point out that single-rotor URANS and VPM simulations of the Ning DJI rotor predict a C_T of 0.122 and 0.125, respectively, meanwhile Zhou et al. report an experimental C_T of 0.1007, leading to a difference of about 20% between the simulations and the experiment. This large discrepancy is believed to be caused by an incomplete description of the rotor geometry (our interpretation of the reported geometry may have differed from that used in the experiment). Additionally, Zhou et al. report an abnormally large standard deviation of C_T in the isolated rotor and its particle-image velocimetry (PIV) shows a skewed streamtube, which suggests that the test stand may have created significant interactions in the flow field. Consequently, we will limit our validation to only a qualitative comparison between predicted and experimental results.

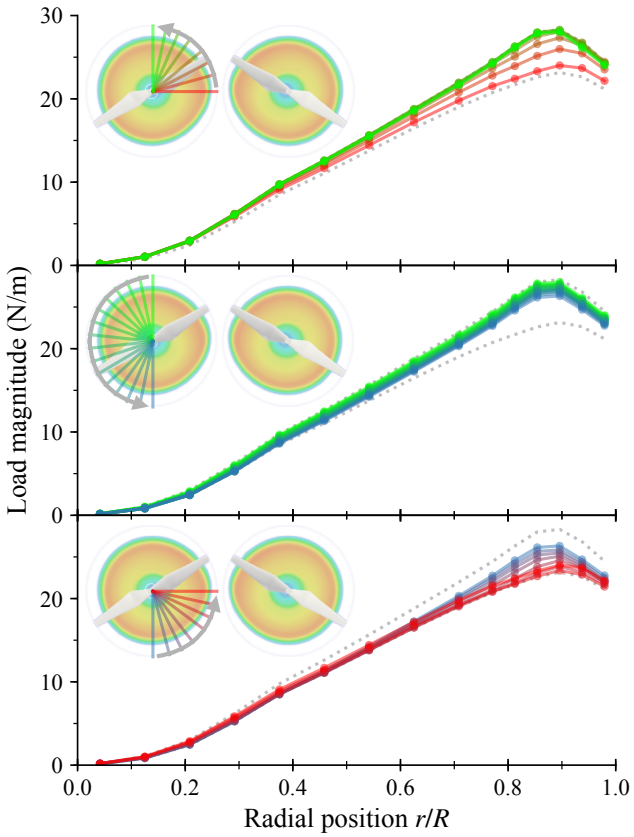

Figure 14: Blade loading dropping as blade goes through region of wake skewness and accentuated upwash in between the rotors.

Aerodynamic interactions between the rotors introduce strong thrust fluctuations as observed in Fig. 12, which shows the instantaneous average between the two rotors at $d = 0.05D$ in the simulations and the measured mean C_T of the experiment. Upon convergence, URANS and VPM simulations predict C_T standard deviations of 0.0025 and 0.0057, respectively, while Zhou et al. report an experimental standard deviation of 0.0272 (as previously mentioned, the experiment contains significant interactions with the test stand that contribute to this large fluctuation). Fig. 13 shows the flow field at a distance $0.1D$ behind the plane of rotation as measured through PIV by Zhou et al. (top figure), and predicted by URANS (middle) and VPM (bottom). The colormap shows axial velocity, while arrows indicate swirl velocity. As a consequence of wake mixing, both simulations show an accentuated upwash in between the rotors in agreement with the PIV, while the streamtube is distinctly deformed in both the PIV and VPM, but only slightly in the URANS. Fig. 14 shows the loading distribution along one blade as the rotor rotates in the URANS simulation, where it is evident that the loading drops as the blade goes through the region of wake skewness and accentuated upwash, reaching a minimum loading as blades meet.

Acoustic Interactions

The unsteady loading caused by aerodynamic interactions leads to a significant increase in aeroacoustic noise. Zhou et al. (Ref. 5) measured a coherent increase in the SPL of the first seven BPFs as the distance between the rotors is reduced from $d = 1D$ to $d = 0.05D$, as shown in Fig. 15 (top). This increase in tonal noise is also accompanied by a slight increase in broadband SPL. The URANS simulation captures an increase in tonal noise through the first three BPFs while missing the higher frequencies. The VPM simulation also captures this increase in tonal noise, but it seems to over-predict when compared to the URANS and experimental SPL. Also, the VPM seems to capture some higher-frequency content around the tenth BPF, but it is unclear whether this is physically accurate or caused by numerical noise. These interactions captured by the VPM make it a promising method for predicting multirotor noise with reasonable accuracy at a low computational cost.

In spite of the noise increase clearly observed in the SPL spectra, this increase is not apparent under the unweighted OASPL metric. Fig. 16 compares the OASPL between $d = 1D$ and $d = 0.05D$ cases predicted by URANS and VPM, showing no substantial increase in unweighted OASPL, while the experiment (circular markers) shows a slight increase of at most

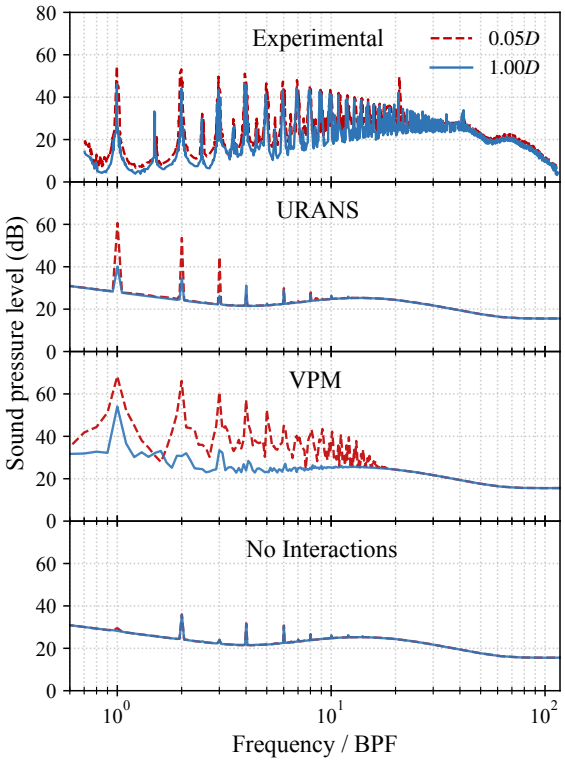

Figure 15: Noise increase at 90° microphone due to rotor-on-rotor interactions as measured experimentally and predicted through URANS and VPM.

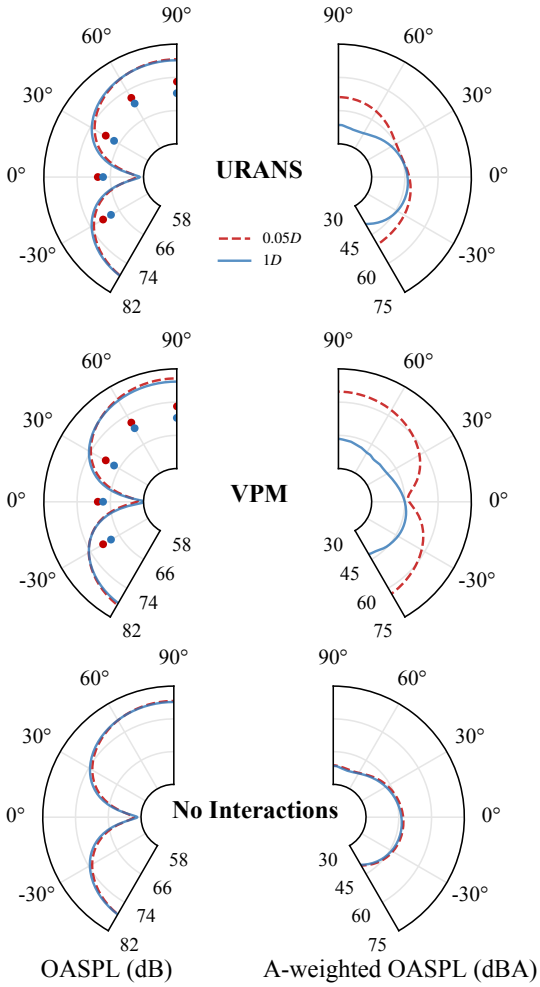

Figure 16: Noise increase due to rotor-on-rotor interactions under unweighted and A-weighted OASPL metrics. Circular markers show the experimental measurements.

3 dB. In fact, in the following section we build a model that ignores all multirotor interactions and show that the unweighted OASPL with this model is indistinguishable from the OASPL of either URANS or VPM. This seems to indicate that the unweighted OASPL is a poor metric of rotor-on-rotor interactions. On the other hand, the increase in noise becomes readily apparent in the A-weighted OASPL, as shown in the right figures of Fig. 16.

Effects of Unsteady Loading

In order to isolate the effects of unsteady loading in multirotor noise, we now build a model that ignores all aerodynamic rotor-on-rotor interactions. The loading of the single-rotor URANS simulation is used as the load of the two rotors, thus superimposing the acoustic pressure radiated by each rotor while capturing no aerodynamic interactions. Without interactions, the spectra at $d = 0.05D$ and $d = 1D$ become indistinguishable from each other, as shown in Fig. 15 (bottom), whereas the URANS spectra had previously shown a noise increase as large as 20 dB in the first three BPFs. The no-interaction model shows an A-weighted OASPL that is indifferent to the separation between rotors (Fig. 16, bottom), meanwhile URANS shows an increase in A-weighted OASPL as large as 12 dBA in some directions. This exercise points out that lower-fidelity models that ignore rotor-on-rotor aerodynamic interactions (like conventional blade-element momentum theory) can erroneously underpredict tonal SPL and A-weighted OASPL by as much as 20 dB and 12 dBA, respectively, when the rotors are close to each other.

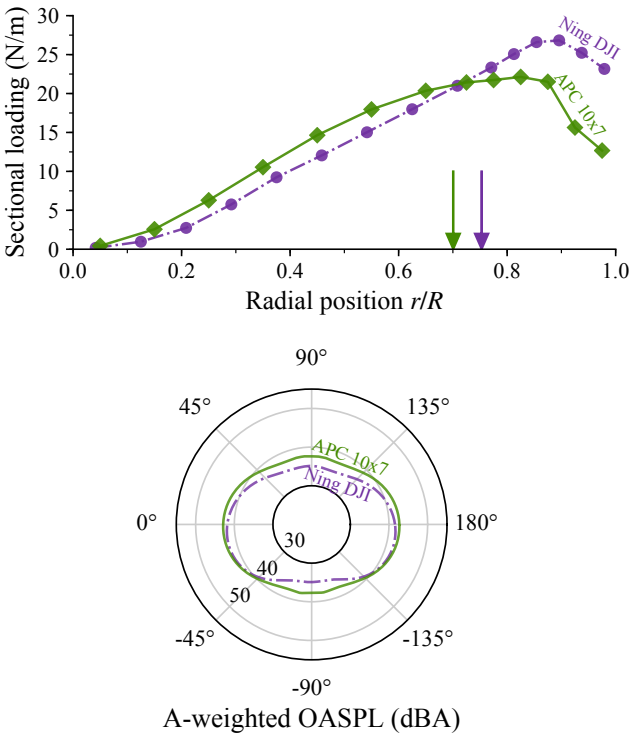

Figure 17: *Top:* Blade loading distribution in single-rotor. Arrows indicate the respective center of pressure. *Bottom:* Noise directivity of single-rotor.

Effects of Loading Distribution

We originally conjectured that the strength of rotor-on-rotor interactions is related to the strength of vortices shed off blade tips. If this hypothesis were true, then a set of rotors with lighter tip loading might experience weaker interactions. In order to test this, the following sections will run sweeps of interactions with both a set of weakly-tip-loaded rotors (APC 10x7) and a set of heavily-tip-loaded rotors (Ning DJI). In order to make both sets comparable, the RPM of the APC 10x7 is tailored to match the thrust of the Ning DJI in single-rotor operation. This is achieved using an RPM of 4660 in the APC 10x7 and 4850 in the Ning DJI, resulting in 3.155 N and 3.123 N of thrust, respectively, and a difference of only 1%. The rotors have approximately the same diameter (the difference is only 14 mm). Fig. 17 (top) compares the resulting loading distribution of both rotors, showing that the center of pressure in the APC 10x7 blade is closer inboard than in the Ning DJI blade. Fig. 17 (bottom) compares the OASPL of both rotors in single-rotor operation, showing that even though the APC 10x7 is about 2 dBA louder than the Ning DJI above and below the rotor, they have a comparable OASPL at $-45°$ below the plane of rotation. Using these RPMs, the following sections report the rotor-on-rotor interactions encountered by the two sets of rotors at the $-45°$ microphone.

Effects of Tip-to-Tip Distance

In order to explore the effects of tip-to-tip distance d on rotor-on-rotor interactions, we now sweep this distance between $d = 1D$ and $d = 0.05D$ using URANS on sets of Ning DJI and APC 10x7 rotors. Fig. 18 shows that the mean thrust drops in between 1% to 2% as the rotors come closer together, in agreement with what Zhou et al. measured experimentally on the Ning DJI rotor (Ref. 5). This is consistent with other studies in the literature (Refs. 2–4, 26, 27) that report a thrust drop of 1% to 4%. Even though this performance drop is arguably negligible, the loading becomes highly unsteady as the rotors come closer together as shown in Fig. 19 (top), with

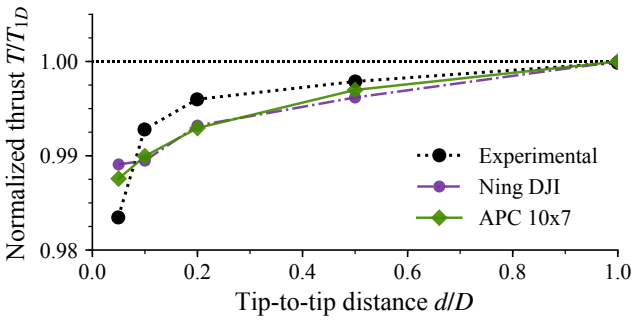

Figure 18: Thrust drop as rotors are brought closer together, normalized by corresponding thrust at $d = 1D$.

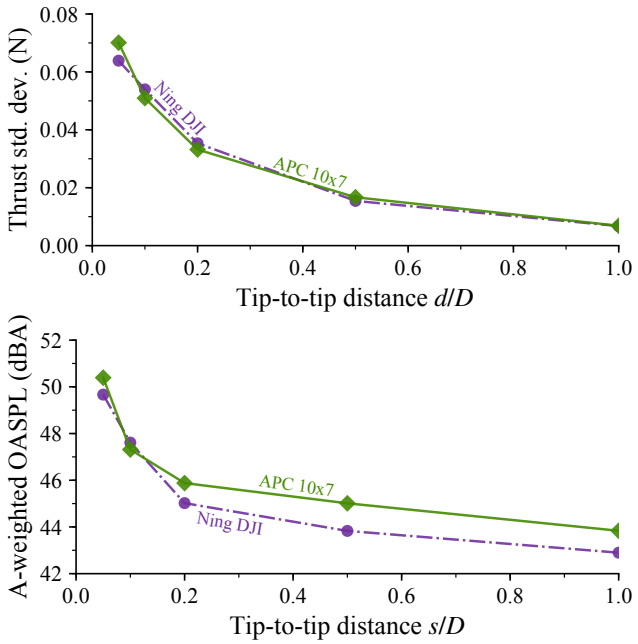

Figure 19: Thrust fluctuation (top) and noise increase (bottom) at -45° microphone as the tip-to-tip distance between rotors is reduced, showing that thrust fluctuation and multirotor noise are closely related.

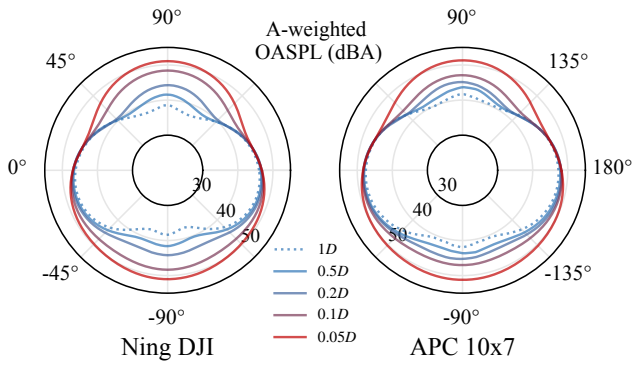

Figure 20: Noise directivity as the tip-to-tip distance d between rotors is decreased.

the thrust standard deviation increasing by a factor of ten between $d = 1D$ and $d = 0.05D$ on both the Ning DJI and the APC 10x7 set. This increase in thrust fluctuation has a direct effect on noise, as shown in Fig. 19 (bottom), increasing the A-weighted OASPL of the -45° microphone by about 7 dBA. Furthermore, the trends in Fig. 19 show that fluctuation and noise are directly related, making the thrust fluctuation a good surrogate metric for rotor-on-rotor noise during design of aircraft with closely-spaced rotors.

Fig. 20 shows the noise directivity as the rotors are brought closer together, evidencing that rotor-on-rotor interactions increase the noise in the axial direction. The noise increase is the strongest both directly above and below the rotors, increasing by about 10 dBA directly underneath. Thus, in eVTOL vehicles, the clearance between rotors and associated

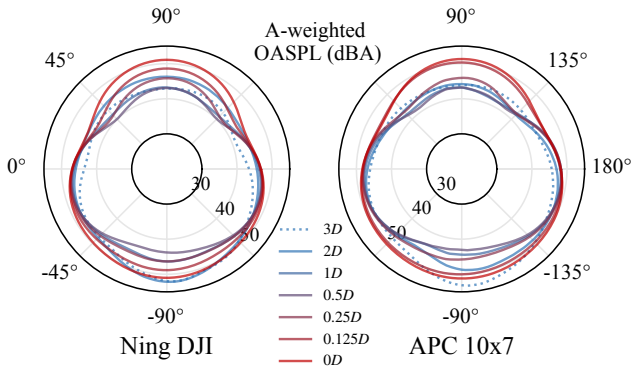

Figure 21: Noise directivity as the downstream spacing s between rotors is varied.

noise must be carefully considered during design since these vehicles typically hover over urban zones during landing and takeoff.

Finally, notice that the interactions in Figs. 18 to 20 show no remarkable differences between the Ning DJI and APC 10x7 rotor sets, which indicates that the lighter tip loading of the APC 10x7 does not alleviate the multirotor interactions.

Effects of Downstream Spacing

In order to explore the effects of downstream spacing s on the interactions, we now sweep this distance between $s = 0D$ and $s = 3D$ at a constant tip-to-tip distance $d = 0.05D$. Fig. 21 shows the A-weighted OASPL directivity as the right rotor is moved further downstream. At first glance, there is no apparent pattern on how the noise increases or decreases. However, taking a slice of this polar plot as shown in Fig. 22, it becomes evident that there is a close relation between OASPL and thrust fluctuation (the fluctuations shown correspond to the downstream rotor). The spacing of minimum fluctuation ($s \approx 0.5D$) leads to a reduction of about 4 dBA from the $s = 0D$ case. Fig. 23 shows the single-rotor wake, hinting that $s \approx 0.5D$ is in the region where the streamtube is no longer contracting and is about to start expanding due to leapfrogging and breakdown of tip vortices. Fig. 24 shows the average thrust between the rotors, showing that the thrust increases in this region due to the contraction of the streamtube, establishing that both aerodynamic and acoustic interactions are favorable at $s \approx 0.5D$. Thus, multirotor vehicles with close tip-to-tip distance d can achieve a noise reduction as large as 4 dBA without any aerodynamic penalties by simply spacing the rotors in the axial (downstream) direction to position the downstream rotor in this favorable region.

Finally, notice that, as in the previous section, the interactions in Figs. 21 and 22 are not alleviated by the lighter tip loading of the APC 10x7 rotor. This leads us to conclude that loading distribution plays no evident role in the strength of rotor-on-rotor aeroacoustic interactions.

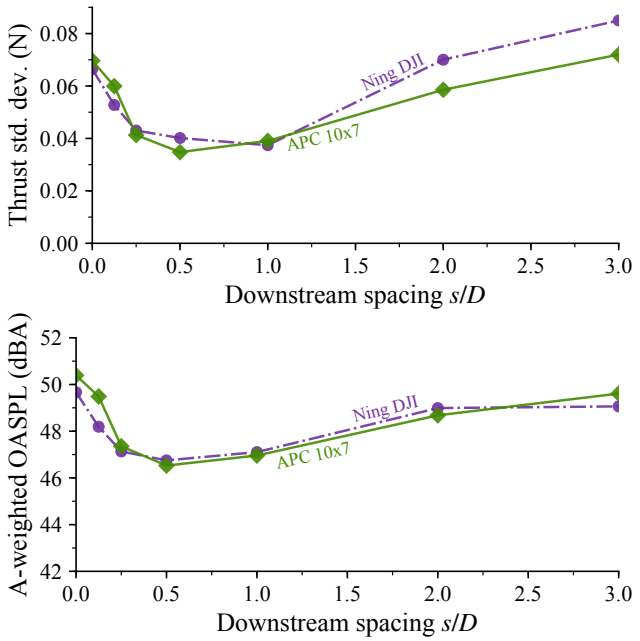

Figure 22: Thrust fluctuation (top) and noise (bottom) at $-45°$ microphone as the downstream spacing between rotors is varied, showing that thrust fluctuation and multirotor noise are closely related.

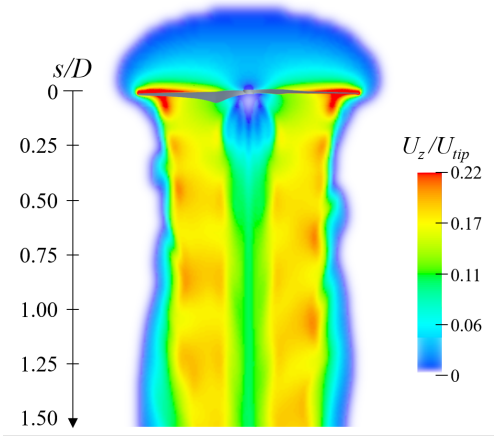

Figure 23: Wake in the Ning DJI single-rotor simulation.

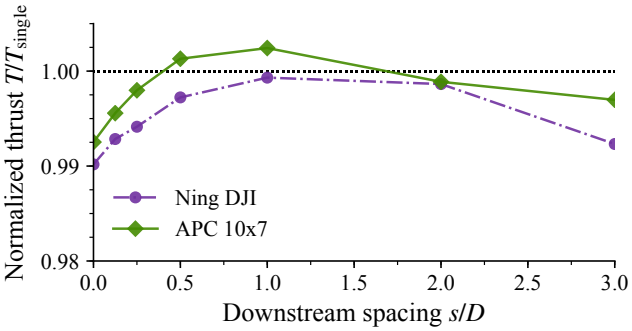

Figure 24: Average thrust between upstream and downstream rotors as the downstream spacing is varied, normalized by thrust of corresponding single-rotor.

CONCLUSIONS

In this study we have characterized the rotor-on-rotor interactions of two counter-rotating, side-by-side rotors in hover as the tip-to-tip distance d and downstream spacing s were varied, leading to the following findings for an observer at a distance of $6D$:

- Noise predictions were validated for single and multirotor configurations, obtaining with the VPM a similar accuracy than the conventional mesh-based methods (URANS and DES) while being two to three orders of magnitude faster.
- Unsteady loading associated with multirotor noise is caused by blade passage through a region of wake skewness and accentuated upwash due to wake mixing in between the rotors.
- Lower-fidelity models that ignore rotor-on-rotor aerodynamic interactions (like conventional blade-element momentum theory) can erroneously underpredict tonal SPL and A-weighted OASPL by as much as 20 dB and 12 dBA, respectively, when the rotors are close to each other.
- Noise caused by multirotor interactions becomes most evident under an A-weighted OASPL metric, leading to an increase in noise as large as 12 dBA as the rotors are mounted closer together.
- Rotor-on-rotor interactions increase the noise the most above and below the rotors, increasing by about 10 dBA directly underneath as the tip-to-tip distance is decreased. Thus, in eVTOL vehicles, the clearance between rotors and associated noise must be carefully considered during design since these vehicles typically hover over urban zones during landing and takeoff.
- Trends of thrust fluctuation and noise show a direct correlation, making the thrust fluctuation a good surrogate metric for rotor-on-rotor noise during design of aircraft with closely-spaced rotors.
- Multirotor noise can be mitigated by spacing the rotors in the axial (downstream) direction to position the tip of the downstream rotor in the region between streamtube contraction and transition to wake breakdown. In our study, the optimal spacing was $s \approx 0.5D$, achieving a noise decrease of about 4 dBA without any aerodynamic penalties.
- The interactions show no sensitivity to blade loading distribution, which indicates that multirotor interactions are not alleviated with a lighter tip loading.

Author contact: Eduardo J. Alvarez ealvarez@byu.edu, Andrew Ning aning@byu.edu.

ACKNOWLEDGMENTS

This work is funded by the High Impact Doctoral Research fellowship granted by Brigham Young University. FLOWVPM uses a modified version of the open-source code ExaFMM originally developed by Lorena Barba and Rio Yokota. FLOWUnsteady integrates the open-source software Paraview as its visualization engine. This study used the aeroacoustics code PSU-WOPWOP developed and facilitated by Kenneth Brentner.

REFERENCES

1. Floros, M. W., "Performance and acoustics of small rotors with non-uniform blade spacing," *The Vertical Flight Society - Forum 75: The Future of Vertical Flight - Proceedings of the 75th Annual Forum and Technology Display*, 2019.

2. Yoon, S., Lee, H. C., and Pulliam, T. H., "Computational Analysis of Multi-Rotor Flows," *54th AIAA Aerospace Sciences Meeting*, , (January), 2016, pp. 1–11. DOI: 10.2514/6.2016-0812

3. Veismann, M., and Gharib, M., "High Fidelity Aerodynamic Force Estimation for Multirotor Crafts in Free Flight," Paper January, AIAA Scitech 2020 Forum, jan 2020. DOI: 10.2514/6.2020-0303

4. Alvarez, E. J., and Ning, A., "Modeling Multirotor Aerodynamic Interactions Through the Vortex Particle Method," AIAA Aviation 2019 Forum, jun 2019. DOI: 10.2514/6.2019-2827

5. Zhou, W., Ning, Z., Li, H., and Hu, H., "An Experimental Investigation on Rotor-to-Rotor Interactions of Small UAV Propellers," *35th AIAA Applied Aerodynamics Conference*, , (June), 2017, pp. 1–16. DOI: 10.2514/6.2017-3744

6. Zawodny, N. S., and Boyd, Jr., D. D., "Acoustic Characterization and Prediction of Representative, Small-scale Rotary-wing Unmanned Aircraft System Components," 72nd American Helicopter Society (AHS) Annual Forum, 2016.

7. Wang, Z., Pandey, A., Sutkowy, M., Harter, B., McCrink, M., Gregory, J. W., and Zhuang, M., "A Comprehensive Approach to Study Aerodynamic and Aeroacoustic Performances of Small Multicopter Unmanned Aerial Systems," *2018 AIAA Aerospace Sciences Meeting*, , (January), 2018, pp. 268. DOI: 10.2514/6.2018-0268

8. Ventura Diaz, P., and Yoon, S., "High-Fidelity Computational Aerodynamics of Multi-Rotor Unmanned Aerial Vehicles," *2018 AIAA Aerospace Sciences Meeting*, 2018, pp. 1–22. DOI: 10.2514/6.2018-1266

9. Abras, J., Hariharan, N. S., and Narducci, R. P., "Wake Breakdown of High-fidelity Simulations of a Rotor in Hover," Paper January, AIAA Scitech 2019 Forum, jan 2019. DOI: 10.2514/6.2019-0593

10. Ventura Diaz, P., Johnson, W., Ahmad, J., and Yoon, S., "The Side-by-Side Urban Air Taxi Concept," Paper June, AIAA Aviation 2019 Forum, jun 2019. DOI: 10.2514/6.2019-2828

11. Mankbadi, R. R., Afari, S., and Golubev, V. V., "Simulations of Broadband Noise of a Small UAV Propeller," Paper January, AIAA Scitech 2020 Forum, jan 2020. DOI: 10.2514/6.2020-1493

12. Schenk, A. R., *Computational Investigation of the Effects of Rotor-on-Rotor Interactions on Thrust and Noise*, Masters thesis, Brigham Young University, 2020.

13. Winckelmans, G., and Leonard, A., "Contributions to Vortex Particle Methods for the Computation of Three-Dimensional Incompressible Unsteady Flows," *Journal of Computational Physics*, Vol. 109, (2), dec 1993, pp. 247–273. DOI: 10.1006/jcph.1993.1216

14. Barba, L. A., Leonard, A., and Allen, C. B., "Advances in viscous vortex methods - Meshless spatial adaption based on radial basis function interpolation," *International Journal for Numerical Methods in Fluids*, Vol. 47, (5), 2005, pp. 387–421. DOI: 10.1002/fld.811

15. Alvarez, E. J., and Ning, A., "Development of a Vortex Particle Code for the Modeling of Wake Interaction in Distributed Propulsion," 2018 Applied Aerodynamics Conference, jun 2018. DOI: 10.2514/6.2018-3646

16. Alvarez, E. J., and Ning, A., "High-fidelity Modeling of Multirotor Aerodynamic Interactions for Aircraft Design," *AIAA Journal (accepted)*, 2020.

17. Alvarez, E. J., and Ning, A., "Unsteady Mixed-fidelity Aerodynamics Solver for Maneuvering Multirotor Aircraft," AIAA SciTech 2021 Forum (in progress), 2021.

18. Brentner, K. S., and Farassat, F., "Modeling aerodynamically generated sound of helicopter rotors," *Progress in Aerospace Sciences*, Vol. 39, (2-3), 2003, pp. 83–120. DOI: 10.1016/S0376-0421(02)00068-4

19. Zolbayar, B.-E., "Investigation of Noise From Electric, Low-Tip-Speed Aircraft Propellers," *The Pennsylvania State University*, , (August), 2018.

20. Brooks, T. F., Pope, D. S., and Marcolini, M. A., "Airfoil self-noise and prediction," Technical report, National Aeronautics and Space Administration, 1989.

21. Ning, Z., *Experimental investigations on the aerodynamic and aeroacoustic characteristics of small UAS propellers*, Ph.D. thesis, Iowa State University, Digital Repository, Ames, 2018. DOI: 10.31274/etd-180810-6057

22. McCrink, M. H., and Gregory, J. W., "Blade Element Momentum Modeling of Low-Reynolds Electric Propulsion Systems," *Journal of Aircraft*, Vol. 54, (1), 2017, pp. 163–176. DOI: 10.2514/1.C033622

23. Ning, S. A., "A simple solution method for the blade element momentum equations with guaranteed convergence," *Wind Energy*, Vol. 17, (9), jul 2014, pp. 1327–1345. DOI: 10.1002/we.1636

24. Ning, A., "Using Blade Element Momentum Methods with Gradient-Based Design Optimization," *(in review)*, 2020.

25. McKay, R. S., and Kingan, M. J., "Multirotor unmanned aerial system propeller noise caused by unsteady blade motion," *25th AIAA/CEAS Aeroacoustics Conference, 2019*, , (May), 2019. DOI: 10.2514/6.2019-2499

26. Shukla, D., Hiremath, N., and Komerath, N. M., "Low Reynolds Number Aerodynamics Study on Coaxial and Quad-Rotor," *2018 Applied Aerodynamics Conference*, 2018. DOI: 10.2514/6.2018-4118

27. Shukla, D., and Komerath, N., "Multirotor Drone Aerodynamic Interaction Investigation," *Drones*, Vol. 2, (4), 2018, pp. 43. DOI: 10.3390/drones2040043